Shallow-Water Flow past Isolated Topography. Part II: Transition to Vortex Shedding

CHRISTOPH SCHÄR* AND RONALD B. SMITH

Department of Geology and Geophysics, Yale University, New Haven, Connecticut

(Manuscript received 3 January 1992, in final form 13 July 1992)

ABSTRACT

The formation of Kármán vortex streets is studied within the framework of single-layer shallow-water dynamics and in absence of surface friction and background rotation. In the first part of this study, steady numerical solutions for flow past circular topography were obtained by imposing a symmetry condition that essentially suppressed vortex shedding. In the second part, this symmetry condition is relaxed in order to study the transition into the vortex-shedding regime.

This transition is due to an instability of the symmetric wake pattern. The most unstable global normal mode of this instability is derived by a numerical method. Most of the features of this mode can be understood in terms of the absolute instability theory. The mode is essentially barotropic and relies on a positive feedback between the perturbations located on the two shearlines on either side of the wake. The classical shear modes centered on a single shearline are, on the other hand, shown to be absolutely stable even though their convective growth rates are substantial. It is also shown that a recently suggested frequency selection criteria pertaining to absolute instabilities in slowly varying shear flow successfully predicts the growth rate of the most unstable global normal mode.

Finite-difference numerical simulations are utilized to trace the evolution of the most unstable global normal mode. It is demonstrated that the evolution to finite amplitude of the most unstable global normal mode leads to the breakup of the steady wake into an oscillating Kármán vortex street. The frequency of eddy shedding in the numerical simulations agrees well with that from observations of eddies behind mountainous islands.

1. Introduction

In this two-part study we have investigated shallow-water flow past circular topography in absence of surface friction. In Part I (Schär and Smith 1993), a symmetry condition was enforced that essentially suppressed vortex shedding. In the Part II, we now relax this symmetry condition and allow for an instability that breaks up the steady wake into an oscillating Kármán vortex street.

An underlying motivation of both Parts I and II is to consider inviscid or pseudoinviscid mechanisms for wake formation. By "pseudoinviscid" we mean that the ideal fluid conservation laws are violated only in discontinuous hydraulic jumps or shocks. Furthermore, the control parameters for such a flow: the ratio of mountain height to fluid depth $M = h_{\max}/H_\infty$ and the Froude number $\mathrm{Fr} = U_\infty(g^* H_\infty)^{-1/2}$, do not contain the viscosity. In Part I, steady separated wake flows were achieved that—while appearing analogous to two-dimensional viscous flows with a separated boundary layer—were different in a fundamental way. As we consider the unsteady problem we will continue to ask whether our flows have a true pseudoinviscid nature.

A second objective is to see whether the pseudoinviscid shallow-water theory of vortex shedding agrees in any way with observations of atmospheric vortex streets (e.g., Nickerson and Dias 1981; Etling 1989; see also the reviews by Atkinson 1981; Chopra 1973) and with the theory of vortex shedding in two-dimensional homogeneous (Hannemann and Oertel 1989) and atmospheric flows (Smith 1989).

In analyzing the mechanism of wake instability in shallow-water flow, we will turn to the theory of absolute instability in a downstream-developing shear flow. This theory takes into account not only the ability of a disturbance to draw energy from the mean flow—as in traditional temporal instability theory—but also the loss of energy from the unstable region by advection or propagation. Reviews of this subject are given by Merkine and Shafranek (1980), Pierrehumbert (1984), and Huerre and Monkewitz (1990). In some respects our treatment follows that of Hannemann and Oertel (1989). Our terminology follows that of Huerre and Monkewitz. In a flow field where the velocity profile is nonuniform in the streamwise direction, the terms "local" and "global" refer to the instability of the local

* Present affiliation: Atmospheric Physics ETH, Zürich, Switzerland.

Corresponding author address: Christoph Schär, Atmospheric Physics ETH, ETH Hönggerberg, 8093 Zürich, Switzerland.

velocity profile and of the entire flow, respectively.[1] Locally, the flow can be "absolutely" or "convectively" unstable, depending on whether the local velocity profile supports stationary growth (absolute instability) or whether growing disturbances are swept away from the source (convective instability). Recent theoretical work has established relationships between local and global instability properties. In particular, the question of whether a confined region of absolute instability implies global instability has obtained considerable attention (Pierrehumbert 1984; Huerre and Monkewitz 1990).

The outline for this paper is as follows: In section 2, the most unstable normal mode is derived using a numerical technique based on the natural selection of the fastest growing mode. Section 3 contains an analysis of the mode in terms of the absolute instability theory. In section 4 numerical simulations are presented that depict the nonlinear evolution of the instability. The study is summarized in section 5, which also includes a short discussion of the relationship between shallow-water and continuously stratified flows.

2. Basic state and global normal mode

The framework for this study has been defined in section 2 of Part I. For the present purpose, we concentrate on one particular flow situation characterized by a dimensionless mountain height $M = 2$ and an upstream Froude number $\mathrm{Fr}_\infty = 0.5$. This case was previously discussed for the near-mountain field by the use of high-resolution simulations in Part I. For the current purpose, a comparatively low resolution of $\Delta x = \Delta y = 0.2$ is employed, which allows for sufficiently large full-space computations without requiring exceedingly large computational costs.

The left–right symmetric steady state under consideration is shown in Fig. 1. It is characterized by a positive (negative) shearline to the right (left) of the wake. The wake consists of two symmetric recirculation bubbles and exhibits a region of reversed flow. The fluid in the wake has reduced values of the Bernoulli head, and some of this fluid escapes at the end of the wake to form a tail that is dissolved by diffusion farther downstream. The alongflow scale of these features is dependent upon the Reynolds number in a similar way as the wake behind a blunt body in homogeneous flow. Low viscosity (high Reynolds numbers) favors the formation of elongated wakes (e.g., Batchelor 1967). Similarly, as will be shown in the present section, long wakes exhibit a high potential for instability and subsequent breakup into a Kármán vortex street.

For the following, the flow of Fig. 1 represents the basic state. The most unstable normal mode is obtained by a numerical technique based on the natural selection of the fastest growing mode. The global normal modes can be cast into the form

$$H' = \mathrm{Re}[\hat{H}(x, y)e^{-i\omega t}],$$
$$u' = \mathrm{Re}[\hat{u}(x, y)e^{-i\omega t}], \quad v' = \mathrm{Re}[\hat{v}(x, y)e^{-i\omega t}], \quad (1)$$

where $\hat{H}$, $\hat{u}$, $\hat{v}$, and ω denote the complex structure functions and the frequency, respectively. Owing to the symmetry of the basic state, the operation ($y \to -y$, $v' \to -v'$) conserves the frequency. The left–right symmetric part of the mode, which is defined by

$$\hat{H}_s(x, y) = \frac{1}{2}(\hat{H}(x, y) + \hat{H}(x, -y)),$$
$$\hat{u}_s(x, y) = \frac{1}{2}(\hat{u}(x, y) + \hat{u}(x, -y)),$$
$$\hat{v}_s(x, y) = \frac{1}{2}(\hat{v}(x, y) - \hat{v}(x, -y)), \quad (2)$$

is again a global normal mode. Since the symmetric basic state is stable with respect to symmetric perturbations (otherwise no steady state would emerge from the simulations of Part I), we can require that the symmetric part (2) of an unstable global mode must disappear, or alternatively, that the structure functions in (1) must satisfy

$$\hat{H}(x, y) = -\hat{H}(x, -y), \quad \hat{u}(x, y) = -\hat{u}(x, -y),$$
$$\hat{v}(x, y) = \hat{v}(x, -y). \quad (3)$$

This feature simplifies the numerical search for the most unstable global normal mode. The search involves a long-term numerical integration with the nonlinear numerical model in the full computational domain (for a description of the numerical model see Part I). The initial conditions are provided by the symmetric basic state perturbed by small amplitude random noise. Every 30 time steps the perturbation, which is according to (3) defined as

$$H'(x, y) = \frac{1}{2}(H(x, y) - H(x, -y)),$$
$$u'(x, y) = \frac{1}{2}(u(x, y) - u(x, -y)),$$
$$v'(x, y) = \frac{1}{2}(v(x, y) + v(x, -y)), \quad (4)$$

is normalized to small amplitude. This assures that the model operates in the range of validity of linear theory. In practice, we have required that

$$\max|H'| < 10^{-4}H_\infty. \quad (5)$$

The use of (4) allows for the basic state to slightly adjust itself to the (previously not employed) full-space geometry. This adjustment is very small and negligible. Alternatively, instead of using (4), the perturbation can be defined as the deviation from the initialized basic state. It was verified that the same normal mode

[1] In the work on absolute baroclinic instability (e.g., Pierrehumbert 1984) the terms "local" and "global" are used differently.

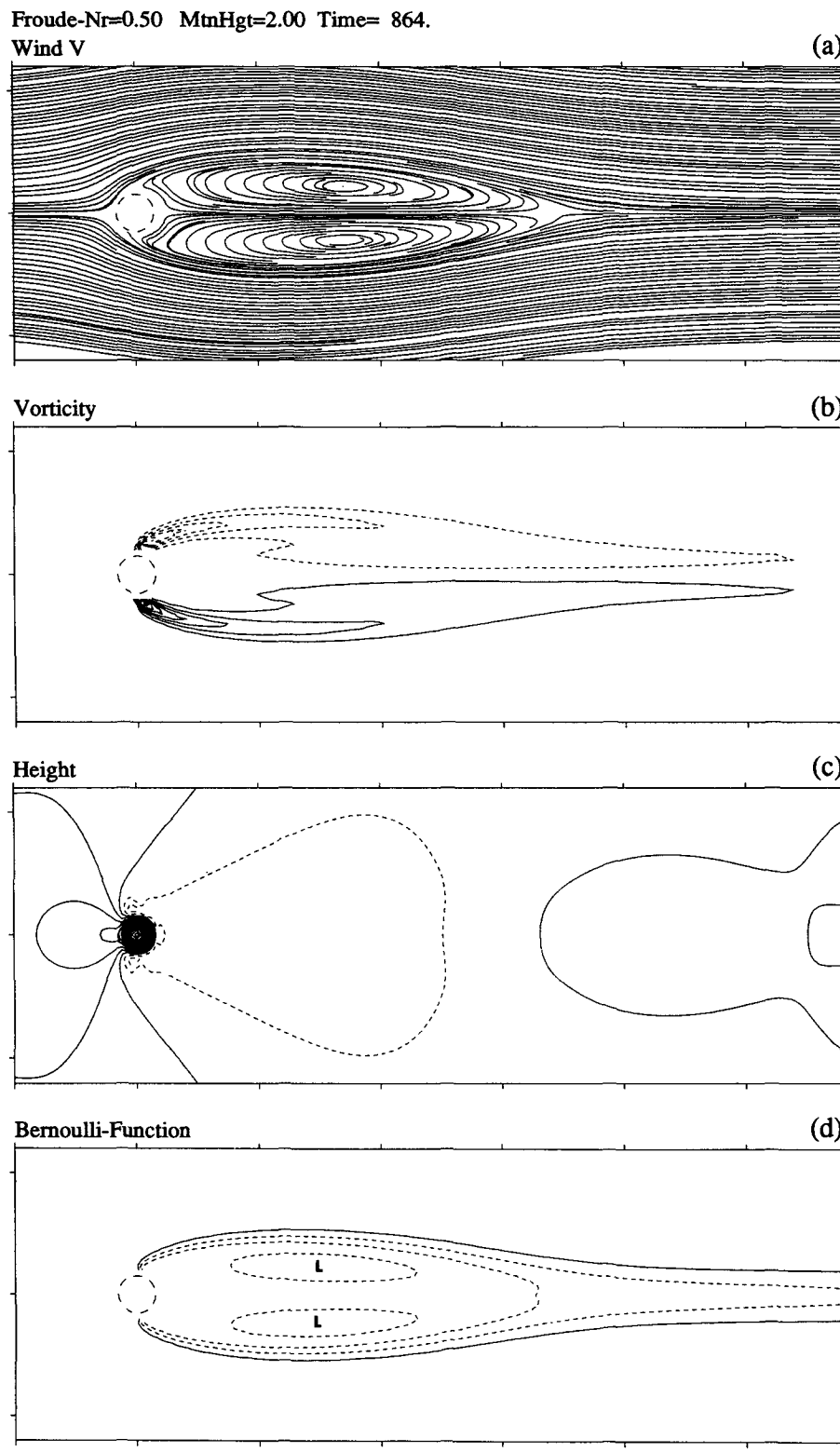

FIG. 1. Steady-state left–right symmetric flow with upstream Froude number $Fr_\infty = 0.5$ past a circular mountain with dimensionless height $M = 2$. The panels show (a) streamlines, (b) vorticity, (c) height of the fluid layer, and (d) the Bernoulli function. The contour intervals are (b) 0.25 with negative contours dashed and zero contour suppressed; (c) 0.05 with contours smaller than the upstream height $H_\infty = 1$ dashed, and (d) 0.0625 with contours smaller the upstream value $B_\infty = 1.125$ dashed. Tick marks are shown every five units.

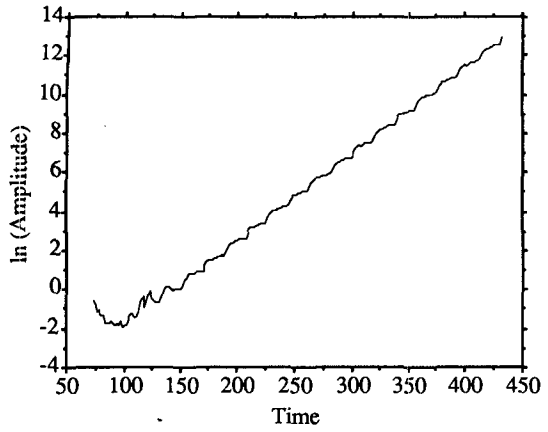

FIG. 2. The logarithmic amplitude $\max(|H'|)$ of the nonnormalized perturbation during the normal-mode search.

evolves. However, this latter procedure requires a highly symmetric version of the code. Otherwise, the numerical method tends to amplify marginal asymmetries of the code, which can on occasion overpower the most unstable normal mode.

The evolution of the (unnormalized) perturbation amplitude is summarized in Fig. 2 in terms of the logarithm of $\max|H'|$. After an initial transient phase, the growth becomes exponential. The superposed periodic fluctuation is due to the change in structure of the mode during the passage of one period. The dimensionless growth rate $\omega_{G,i}$ amounts to 0.45 and the period is 37.2.

The mode is displayed in Fig. 3 for one particular phase. The dashed line is a contour of the basic-state vorticity, while the dotted and full lines refer to contours of the most unstable normal mode. During one period, the mode continuously changes its structure. The individual features of the mode first appear with small amplitude to the immediate lee of the mountain, then propagate downstream and experience growth. The extremes of the various fields occur near the downstream stagnation point of the wake. Farther downstream, they are subject to decay with respect to the whole field, which grows accordingly to the global growth rate.

Unlike the classical instability analysis, the global analysis avoids an explicit specification of a wavelength [see Eq. (1)]. However, it is apparent that the most unstable normal mode is characterized by a rather well-defined wavelength, whose scale and related phase velocity is provided in Table 1 for later comparison.

3. Nature of the instability

In this section we attempt to explain the growth of periodic wake oscillations found in the numerical model in the previous section. We hope to explain the growth rate, period, and location of the sinuous perturbation found in the full-space calculations and the apparent stability of the half-space calculations with left–right symmetry (LRS). For this purpose we turn to the theory of absolute instability in a slowly varying shear flow. We begin by extracting from the LRS numerical calculations the family of wake velocity profiles $u(y; x)$, where x appears as a parameter. The linear stability of each profile is examined under the assumptions that the flow is inviscid, nondivergent, and that the $u(y; x)$ profile can be treated as a homogeneous parallel shear flow. For a disturbance of the form

$$v(x, y, t) = \hat{v}(y)e^{i(kx-\omega t)}, \tag{6}$$

we have the eigenvalue problem

$$\hat{v}_{yy} - \left(\frac{u_{yy}}{u-c} + k^2\right)\hat{v} = 0, \tag{7}$$

with

$$\hat{v}(y = \pm D) = 0 \tag{8}$$

at the lateral edge of the domain. The wavenumber, frequency, and phase speed $c = \omega/k$ are considered to be complex (Drazin and Reid 1981). The inviscid assumption arises from our estimate that the numerical dissipation in the model is small, corresponding to a Reynolds number of at least 80. The nondivergent assumption arises from the observation that the depth variations associated with the growing instability are small in the numerical model runs.

For each value of k, the eigenvalue c in (7) is found by an iterative shooting technique, integrating (7) from $y = 0$ to $y = D$ and altering c until (8) is satisfied. At $y = 0$, the conditions

$$\hat{v} = 1 \quad \text{and} \quad \hat{v}_y = 0 \tag{9}$$

are used for the sinuous disturbance, while

$$\hat{v} = 0 \quad \text{and} \quad \hat{v}_y = 1 \tag{10}$$

are used for the varicose disturbance satisfying the LRS condition. The result of this procedure, applied to each wake profile, is a complex dispersion relation

$$\omega(k; x) \tag{11}$$

in which x appears as a parameter. An example of a dispersion relation for $x = 12$ using (9) is given in Fig. 4. From such a diagram, the maximum convective growth rate can be determined as

$$\omega_{c,i}(x) = \max[\mathrm{Im}\omega(k; x)] \tag{12}$$

with $k_i = \mathrm{Im}k = 0$. The values given by (12) are not directly relevant to our wake stability problem as they represent the growth rate of wave packets that advect or propagate away. They do however represent the efficiency at which energy can be drawn from the wake shear flow by a periodic disturbance. The absolute growth rate can be found from (11) according to

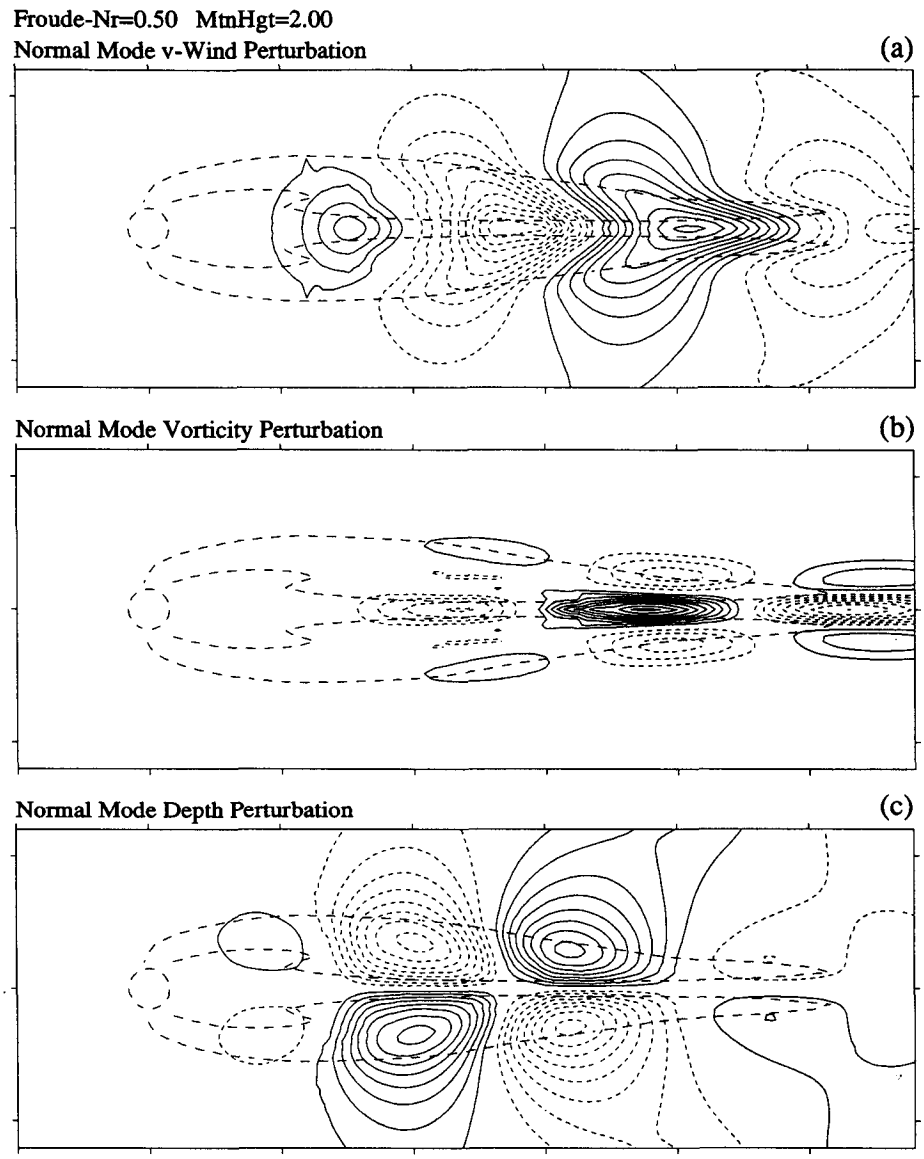

FIG. 3. Structure of the most unstable global normal mode for the flow shown in Fig. 1. The panels show (a) the across-stream velocity component, (b) the vorticity, and (c) the fluid-depth perturbations. The amplitude of the mode is normalized such that $\max(|H'|) = 1$ and all negative contours are dashed. Contour intervals are (a) 0.6, (b) 3.5, and (c) 0.12.

$$\omega_{a,i}(x) = \mathrm{Im}\omega(k_a; x), \tag{13}$$

where k_a is the point in complex wavenumber space where the group velocity

$$\frac{\partial \omega}{\partial k} = 0. \tag{14}$$

The saddle point corresponding to (14) is easily identified in Fig. 4. The disturbance energy associated with wavenumbers near k_a remains in place as it grows. Both the convective and absolute growth rates [from (12) and (13), respectively] are plotted in Fig. 5 as a function of x.

We first consider the sinuous mode (or Kármán mode as it is sometimes called). As expected, the distribution of convective instability along the wake provides little useful information. The typical value for $\omega_{c,i} \approx 0.11$ is more than double the observed global growth rate $\omega_{G,i} = 0.045$. The nearly constant value of $\omega_{c,i}$ with x provides no basis on which to explain the localization of the growth found in the numerical run. The absolute growth rate is more localized, reaching a maximum at $x = 13$ and decreasing rapidly downstream (Fig. 5). The region of positive absolute growth rate is closely linked to the region with reverse flow along the axis (Mattingly and Criminale 1972). Near

TABLE 1. Characteristics of the most unstable global normal mode, the modes derived from the absolute and convective instability analysis, and some of the characteristics during the finite amplitude periodic shedding state. The underlying dimensionless notation is based on the half-width a of the topographic obstacle, and the time scale is $a\mathrm{Fr}_\infty/U_\infty$.

	Frequency	Growth rate	Wavelength	Phase velocity	Period
Linear 2D analysis (section 2)					
global normal mode	0.169	0.045	~12	~0.32	37.2
Linear 1D analysis (section 3)					
convective at $x = 13$	0.165	0.112	11.2	0.29	38.1
absolute at $x = 13$	0.178	0.092	10.6	0.30	35.3
absolute WKBJ	0.17	0.061			37.0
Finite amplitude (section 4)	0.27	0	~10	~0.43	23.0

$x = 18$ the closed wake in the LRS solution has its downstream stagnation point; this point nearly coincides with the end of the absolutely unstable region.

According to Pierrehumbert (1984) and Huerre and Monkewitz (1990), the shape of the growing wave packet envelope can be predicted from the x distribution of $\omega_{a,i}$. The wave amplitude will increase downstream over the range of x where $\omega_{a,i} > 0$, reaching a maximum where $\omega_{a,i} = 0$ (e.g., at $x = 18$). Farther downstream the envelope decays. This description fits the numerical results quite well (compare Figs. 5b and 5c).

There have been several attempts to use the dispersion relation (11), to predict the growth rate and frequency of the global mode. Pierrehumbert (1984), for example, suggested that the maximum value of $\omega_{a,i}(x)$ would approximate the global growth rate. More recently Chomaz et al. (1991, see Huerre and Monkewitz 1990) proposed instead that the complex frequency is governed by the properties of (11) near a saddle point (X_s) in the complex X plane, where

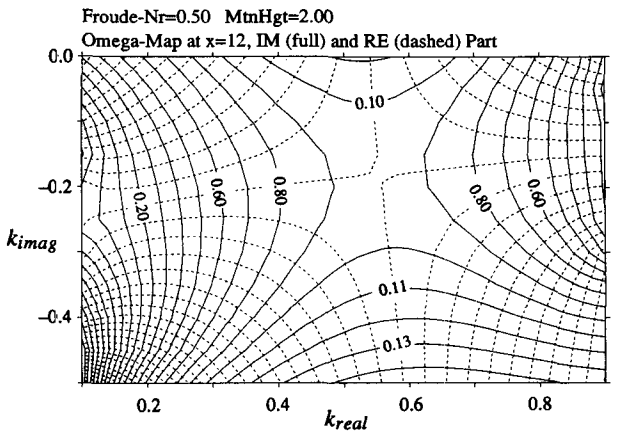

FIG. 4. An example of the ω map for the absolute instability analysis at $x = 12$. Full and dashed contours refer to real and imaginary parts of the complex dispersion relation $\omega(k)$, respectively. The diagram shows the portion of complex k space encompassing the saddle point.

$$\frac{\partial \omega_a}{\partial X} = 0, \tag{15}$$

so that locally

$$\omega_a(X) = \omega_s + \frac{1}{2}\omega_{XX}(X - X_s)^2. \tag{16}$$

The three unknowns in (16), ω_s, ω_{XX}, and X_s, can be determined by analytic continuation using the information along the real x axis. We begin by fitting the real and imaginary parts of ω_a in Fig. 5c,d to quadratic functions

$$\omega_{a,r}(x) = 0.162 + 0.00166(x - 9)^2, \tag{17}$$

and

$$\omega_{a,i}(x) = 0.092 - 0.00306(x - 13)^2. \tag{18}$$

Using (17) and (18) and setting $X = x$ in (16) gives

$$\omega_s = 0.1825 + 0.0808i, \tag{19}$$

$$X_s = 12.09 - 1.68i, \tag{20}$$

and

$$\omega_{XX} = 0.0033 - 0.0061i. \tag{21}$$

The determination of (19), (20), and (21) in this way depends on the assumption that the saddle point X_s is close enough to the real axis that (16) is accurate there. Other important functions can be estimated at X_s by extrapolating linearly off the real x axis using the Cauchy–Riemann equations. For example,

$$k_a(X_s) = 0.56 - 0.11i, \tag{22}$$

$$\partial k_a/\partial X = 0.04 - 0.01i, \tag{23}$$

and

$$\omega_{kk_a}(X_s) = -0.17 - 1.0i, \tag{24}$$

where the corresponding values on the real x axis were taken from ω maps, as shown in Fig. 4.

The WKBJ global frequency formula given by Huerre and Monkewitz (1990) is

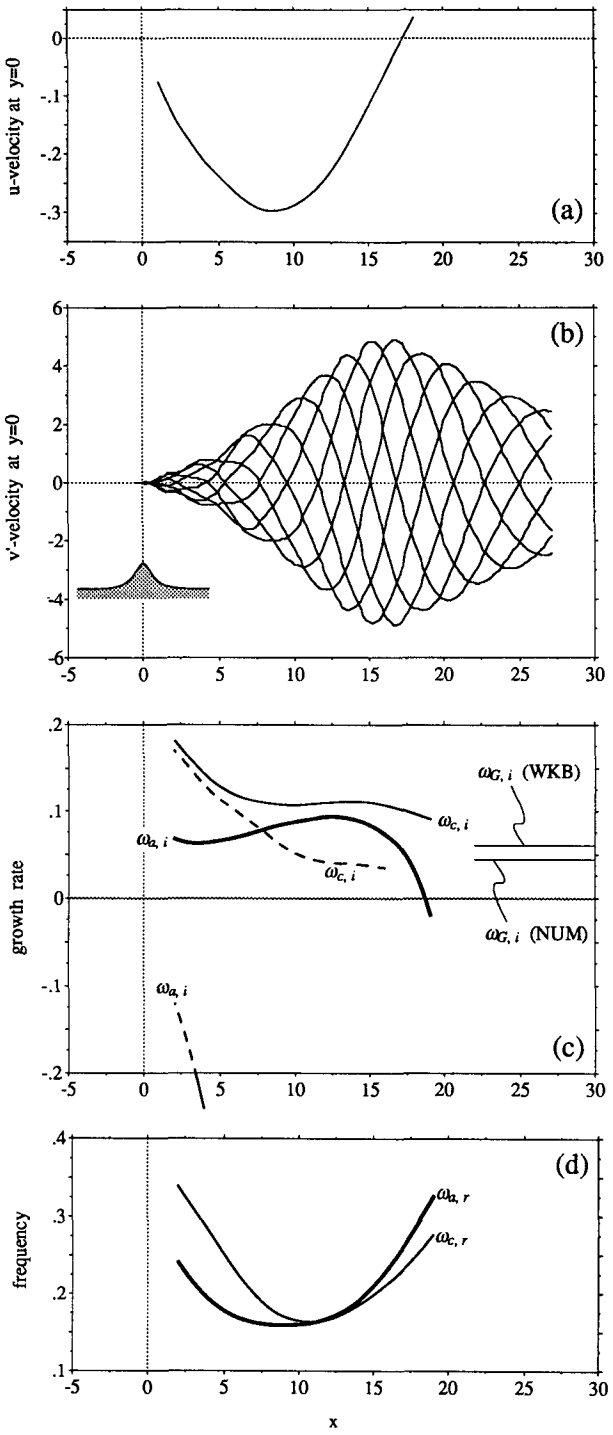

FIG. 5. Results of the absolute instability analysis on the centerline as a function of the alongstream distance downstream from the center of the mountain. Panels (a) and (b) show the alongstream velocity component of the basic-state flow and the across-stream velocity component for eight phases of the most unstable global normal mode. Panels (c) and (d) show the absolute (ω_a) and convective (ω_c) growth rates and frequencies, respectively. Panel (c) in addition displays the global growth rates $\omega_{G,i}$ as obtained from the numerical normal-mode search and the WKBJ expansion. The dashed curves in (c) refer to the absolute growth rates for left–right symmetric modes.

$$\omega_G = \omega_s - \frac{i}{2}\omega_{kk_a}(X_s)k_{aX}(X_s) + \frac{1}{2}(\omega_{kk_a}(X_s)\omega_{XX}(X_s))^{1/2}. \quad (25)$$

The first term in (25) gives the global frequency that would occur if the region of positive absolute growth rate was very long. From (19), this growth rate estimate is $\omega_{s,i} = 0.0808$ compared to the numerical result $\omega_{G,i} = 0.045$. The second and third terms in (25) arise from variation of the stability parameters with x. Idealized interpretations of these terms can be sought by considering the case of wave propagation with all the factors in (25) real. The second term then describes wave amplitude decay due to group velocity divergence,

$$\frac{da^2}{dt} = -\frac{d(C_g a^2)}{dx} = -a^2\omega_{kk}k_x, \quad (26)$$

so that, due to this effect alone,

$$\omega_{G,i} = \frac{1}{a}\frac{da}{dt} = -\frac{1}{2}\omega_{kk}k_x. \quad (27)$$

The third term in (25) represents decay by dispersion of a wave packet. While condition (14) ensures that the wave will not wholly propagate away, it will still spread energy up and downstream as its different wavenumber components have different group velocities according to $\omega_{kk} = \partial C_g/\partial k$. This effect is inversely related to the width of the region of absolute instability $L = 2[-2\omega_s/\omega_{kk}]^{1/2}$.

Substituting (19), (21), (23), and (24) into (25) gives

$$\omega_G = 0.17 + 0.061i. \quad (28)$$

The second term in (25) has only a small effect on (28). The value in (28) compares better with the numerical result

$$\omega_G = 0.17 + 0.045i \quad (29)$$

than did the value of ω_a at $x = 13$ [i.e., the point of maximum $\omega_{a,i}$ on the real axis found from (17) and (18)]. The remaining error in the growth rate ($\approx$25%) is due either to inadequacies of the WKBJ method or to the assumption of inviscid and nondivergent flow in the absolute instability analysis.

The significant reduction in growth rate due to dispersion indicates that a considerable fraction of the energy extracted from the mean shear flow in the absolutely unstable region is exported to adjacent regions. It follows that a region with reversed flow (which will closely correspond to the region of absolute instability) is itself not sufficient to induce global instability. As in homogeneous two-dimensional flow, a short steady wake with recirculation is possible.

Further verification that the eigenvalues of (7) capture the nature of the wake instability is seen by comparing the fields of y velocity

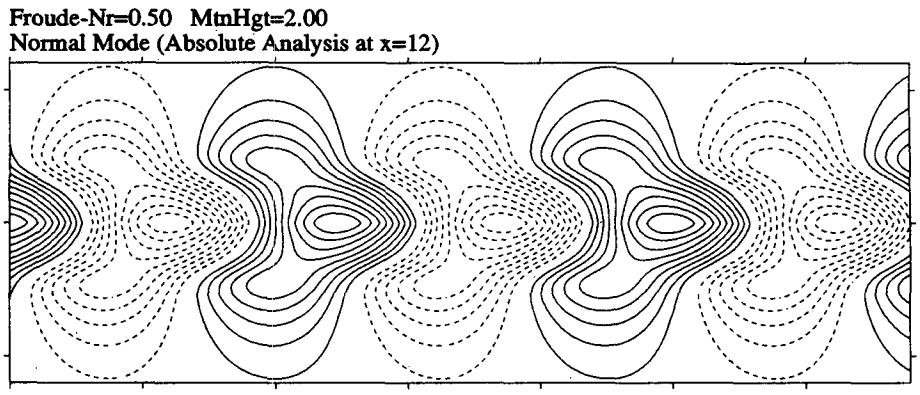

FIG. 6. Across-stream velocity perturbation of the normal mode (30) as derived from the absolute instability analysis at $x = 12$. Conventions as in Fig. 3a.

$$v(x, y) = \mathrm{Re}(\hat{v}(y)e^{ikx}) \qquad (30)$$

for $k = 0.5$ with the numerical results (Figs. 6 and 3a). Both fields show the phase tilt reversal across the symmetry axis required for the disturbance to draw energy from the mean flow by the downgradient flux of momentum.

Finally, we ask why the strategy of finding the LRS solution in the half-space (Part I) and investigating its stability in full-space (Part II) was successful. Why was the LRS solution not unstable in the half-space? It contains inflected velocity profiles and is nearly inviscid, thus satisfying the Rayleigh condition for instability. The answer again lies in the concept of absolute instability.

The effect of LRS on the stability problem can be simulated by replacing (9) with (10). The resulting maximum temporal and absolute growth rates for the varicose mode are shown dashed in Fig. 5c. The profiles are convectively unstable, particularly at $x = 2$, 3, and 4, where the sharp shear layer comes off the hill, but the absolute growth rates are negative everywhere. This result was expected from the earlier results of Huerre and Monkewitz (1985) for a free shear layer. A small disturbance added to the shear layer would draw energy from the shear but propagate quickly away, preventing global growth. This explains the stability of the half-space LRS solution found with the numerical model.

4. Nonlinear evolution and transition to vortex shedding

Next, we discuss the nonlinear evolution of the sinuous instability mode. To this end, the numerical model is initialized with the basic state superposed by the global normal mode as obtained in section 2. The resulting evolution of the vorticity field is displayed in Fig. 7. The initial amplitude of the normal mode at $t = 0$ is very small, and the deviation of the LR symmetry is barely visible. Thereafter, a wavelike oscillation develops, which until $t = 36$ almost exclusively affects the downstream end of the wake. After further growth, individual blobs of vorticity separate from the shearline and are shed into the downstream flow (see $t = 72$ in Fig. 7c). At this time, the shedding occurs at a considerable distance downstream of the mountain. The oscillating perturbation then works its way upstream toward the mountain, and after considerable time has passed, the flow reaches the shedding state. This state is characterized by the alternate shedding on either sides and to the immediate lee of the mountain.

The trace of this evolution at one particular grid point is shown in Fig. 8a. The selected grid point is located on the symmetry axis and within the region of reversed flow (see mark in Fig. 7d). The surface height of the fluid layer and the u and v components of the wind as a function of time are shown by the full, dotted, and dashed lines, respectively. For the current setting, the duration of the transition takes about five shedding periods. During this transition, the alongstream component of the wind switches from the reversed (i.e., $u < 0$) back into the downstream direction. The oscillation in the across-stream direction has roughly the amplitude of the upstream flow (i.e., $U_\infty = 0.5$). After about 10 shedding periods, the oscillation becomes almost perfectly periodic in time, as evident from the blown-up portion of the temporal evolution at the same grid point toward the end of the simulation (Fig. 8b). In order to further illustrate the periodic nature of the oscillation, an additional snapshot of the vorticity field is presented in Fig. 9b, which is taken roughly one half period (i.e., 364 time steps) after the one shown in Fig. 7d. These two diagrams show the shedding of a positive (negative) vortex to the right (left) of the obstacle and exhibit a high degree of symmetry to one another. The additional panels in Fig. 9 show the instantaneous streamlines and the variations of both the height field and the Bernoulli function.

As newly formed vortices break off and begin to drift downstream, their centers are located close to the symmetry axis. Farther downstream, they move apart—positive vortices to the right and negative vortices to the left—possibly approaching the geometry predicted by von Kármán. He recognized that the characteristic

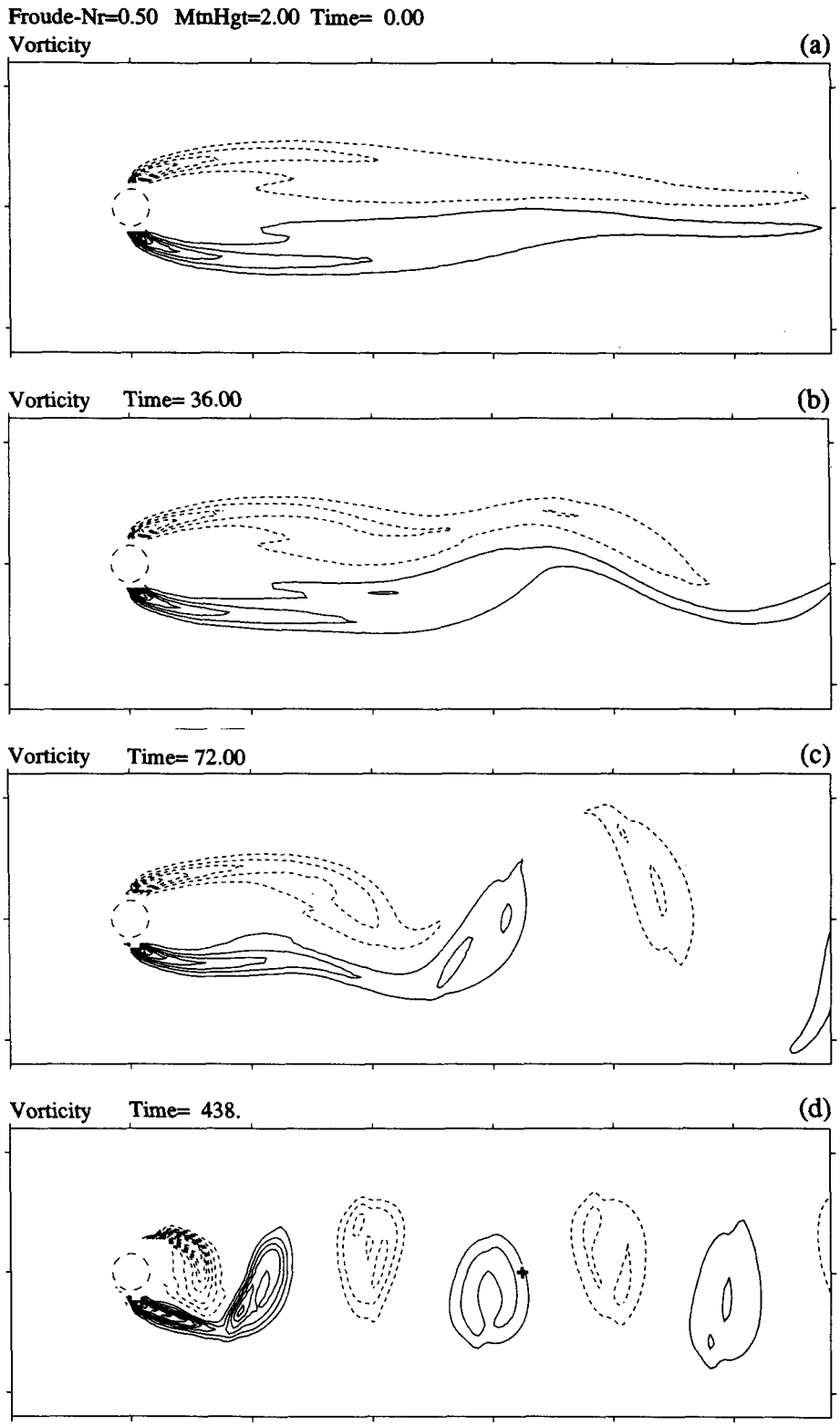

FIG. 7. Nonlinear evolution of the most unstable global normal mode. The panels show the vorticity distribution in the same format as in Fig. 1.

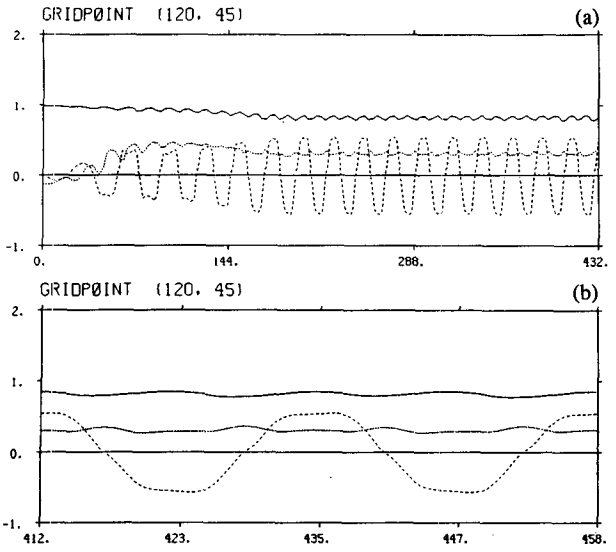

FIG. 8. Trace of the layer depth H (full line), the across-stream velocity component v (dashed line), and the alongstream velocity component u (dotted line) during the nonlinear evolution of the most unstable global normal mode. Panel (b) is a blown-up view of two periods toward the end of the numerical integration. The location of the selected grid point is $(x, y) = (16, 0)$, and is indicated in Fig. 7d.

alignment of the vortices in a vortex street is driven by stability properties. He showed (assuming point vortices, inviscid dynamics, and a vortex street of infinite length) that a stable alignment is obtained only if $b/\lambda = 0.28$, where b and λ denote the distance between the two vortex trains and the distance between vortices of the same train, respectively. A summary of these studies, including comparison with laboratory experiments, can be found in von Kármán and Rubach (1912).

Each individual vortex is accompanied by a dip in the fluid surface that results in a related, roughly circular, region of low pressure. The structure of the vortices is characterized by a balance between the pressure force and the centrifugal force. The generation of the individual vortices to the lee of the obstacle is related to the presence of two hydraulic jumps over the flanks of the mountain. These jumps were already detected in the discussion of the steady-state wake (see Fig. 7 of Part I). However, in the present regime, the two jumps are far from being steady and undergo a periodic movement back and forth accompanied by considerable changes in the strength of the shocks. These changes are linked to the production of different amounts of vorticity on either side of the mountain in the course of one period. For example, during half the cycle, the right-hand flank shock (looking downstream) is strong and produces a stream of fluid with positive vorticity that coils into a developing positive lee eddy. During this time, the left-hand flank is barely discernible.

The shedding period amounts to 731 time steps (23.0 dimensionless units), and this corresponds to 62% of the linear period of the normal mode. This nonlinear modification of the period goes along with a reduction of the predominant wavelength, also apparent in Fig. 7 upon comparison of panels (c) and (d). These values are summarized in Table 1 for comparison with the linear mode. The significant nonlinear effects are not surprising, but directly linked to the deviation of the wake structure from that suggested by the normal mode. In the latter, the growth of the individual vortices was comparatively slow and distributed over the whole length of the wake, while the nonlinear regime is characterized by rapid formation of the vortices in the immediate lee of the mountain and subsequent advection. The mean fields obtained from the time average of the flow over one period (not shown) show that the region with reversed flow has shrunk significantly (as indicated by the trace of u in Fig. 8a). This is consistent with the increased phase velocity during the nonlinear phase as compared to that of the normal mode (cf. Table 1).

The shedding period for the case $M = 2$, Fr = 0.5 discussed above can be compared with observations in the atmosphere. According to the review by Atkinson (1981), the Strouhal number

$$\mathrm{St} = \frac{D}{T_e U}, \tag{31}$$

where D is the island diameter, T_e the period of observed eddy shedding, and U the incoming wind speed, ranges between 0.15 and 0.32. From the present numerical simulations the dimensional value of the shedding period is

$$T_e = 23 a U_\infty^{-1} \mathrm{Fr}. \tag{32}$$

With $D = 2a$ and Fr = 0.5, one obtains St = 0.18, which falls nicely within the observed range.

5. Summary and discussion

In this two-part study, we have investigated the flow of a single layer of shallow water past circular topography with gentle slopes and in absence of surface friction. Our primary motivation for this work arises from observations of wakes in the atmosphere behind mountains. The free surface in our model serves as a surrogate for stratification and is intended to mimic the pronounced inversions often observed in events of atmospheric vortex shedding. While this approach is at best a highly idealized model for atmospheric flow, qualitative comparison with observed features is encouraging. For instance, the occurrence of sharp shear lines that appear immediately to the lee of the mountain has been confirmed by observations taken during the recent Hawaiian Rainband Project (HaRP). It will be one of the aims of the ongoing HaRP data analysis to assess the value of this and other theories of flow past isolated topography. There are also other applications of the theory of shallow flow past obstacles: ocean currents or tidal currents past islands or river flow past boulders or sand bars.

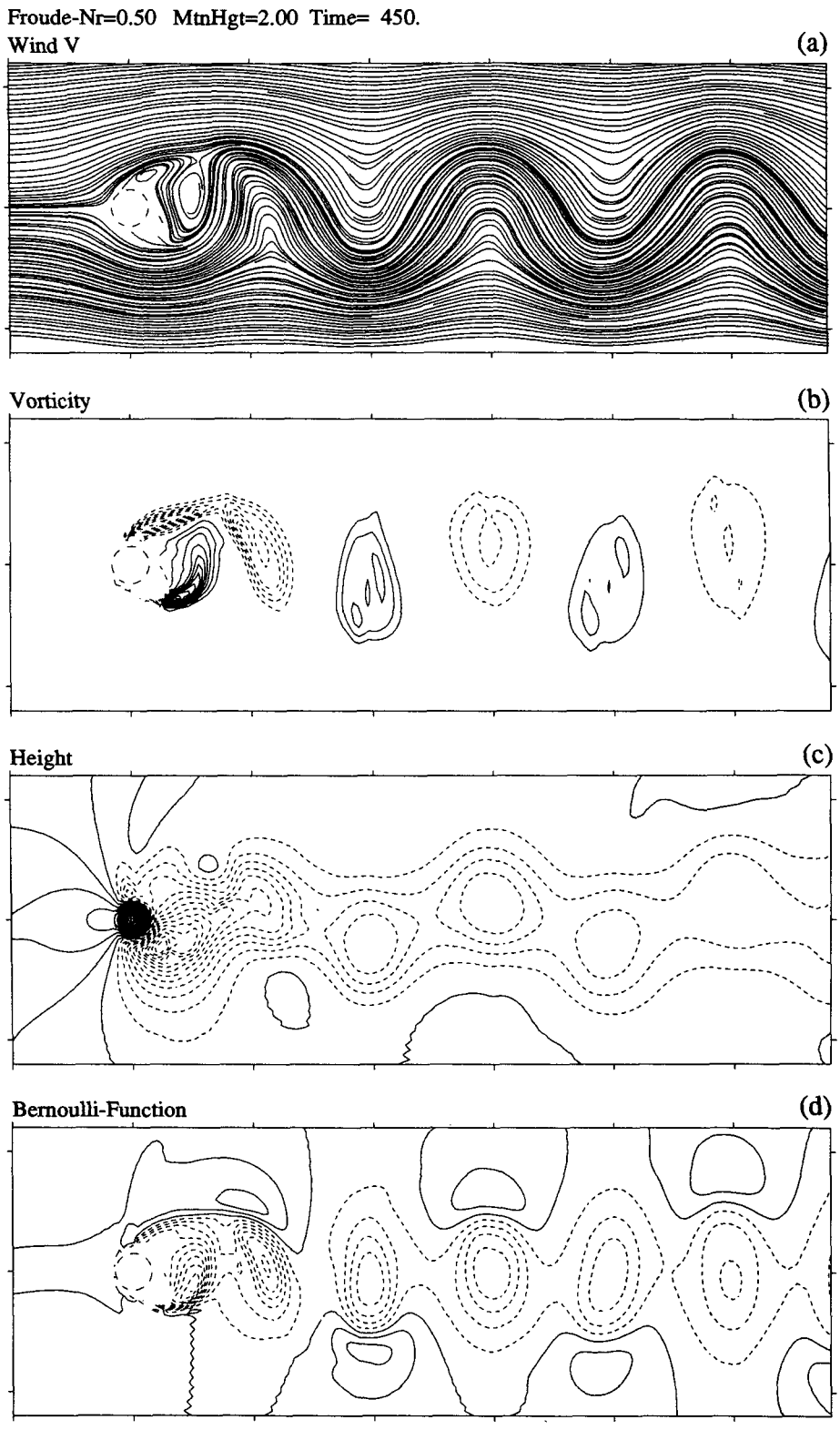

FIG. 9. As in Fig. 1 but for the periodic shedding state.

Major changes in the flow structure occur as the dimensionless mountain height is raised beyond some critical value that depends on the Froude number. At this point, hydraulic jumps appear, which create potential vorticity and a wake structure. The presence of these potential vorticity anomalies renders the flow potentially susceptible to barotropic instabilities. With small lateral viscosity, the wake becomes elongated with reverse flow. This allows for an instability that breaks the left–right symmetry of the problem. It was demonstrated that the nonlinear evolution of this instability breaks up the steady wake into an oscillating Kármán vortex street. Surprisingly quickly, this nonlinear oscillation becomes perfectly periodic in time. Each shed vortex is composed of a coiled stream of vortical fluid coming from jumps of alternating strength on the flanks of the hill. The computed shedding frequency agrees with atmospheric observations.

In analyzing the linear phase of the wake instability, we made use of a recently suggested frequency selection criteria in the absolute instability theory of slowly varying shear flows (see Chomaz et al. 1991). This method is based on a WKBJ treatment of the variation in the streamwise direction and predicts the global growth rate solely based on local instability considerations. The most unstable global normal mode relies on the interaction of perturbations near the two shear lines that encompass the wake. This behavior can also be understood in terms of absolute instability theory. While the individual shearlines clearly satisfy the criteria for barotropic instability, each on its own, the associated convective modes quickly export the perturbation energy away from the regions of significant shear, rendering these modes absolutely stable. Absolute instability essentially requires that the modes are able to couple with the reverse flow on the centerline of the wake.

The analysis in this paper has concentrated on one particular case, characterized by high topography that pierces the fluid surface. This flow belongs to regime III according to the classification given in Part I. We have repeated the analysis for one particular case of regime IIb (defined by $\mathrm{Fr}_\infty = 0.5$ and $M = 0.8$), where the mountain is entirely submerged. This latter case proved to be unstable as well and broken up into a Kármán vortex street. This result is not surprising since both of these regimes are associated with pronounced and elongated bands of potential vorticity as well as with a region of reversed flow. It can hence be expected that most of the regimes IIb and III will give rise to vortex shedding.

Vortex shedding in the shallow-water equations is the result of an essentially pseudoinviscid mechanism. In Part I, with wake instabilities suppressed by a symmetry condition, the closed wake circulation allowed for some influence of lateral viscosity in determining the length of the wake bubble. In Part II, we have come closer to the pseudoinviscid limit as the wake with shedding eddies is repeatedly flushed with new fluid from upstream, preventing any slow cumulative effect of viscosity.

The remarkable geometrical similarity between pseudoinviscid wakes and wakes in 2D viscous flow is due to two things. First, in both models vorticity is produced near the hill slopes. In 2D viscous flow the vorticity is due to a no-slip condition and viscous diffusion of vorticity. In the pseudoinviscid model, the vorticity is produced in the very shallow water on the hill slopes where the local Froude number exceeds unity and thus allows jump formation. The second similarity is that vorticity advection works identically in the two models. The nature of vorticity advection is responsible for phenomena ranging from linear shear instability to the establishment of the Kármán vortex street.

Acknowledgments. We wish to thank Edward W. Bolton, who brought to our attention some of the work on absolute instability theory in homogeneous flow past blunt bodies. Peter Monkewitz advised us on the application of WKBJ theory to our results. This study was started while CS was the recipient of a postdoctoral fellowship from the Swiss National Science Foundation. Further support has been provided by NSF under Grants ATM-8914138 and ATM-9106494.

REFERENCES

Atkinson, B. W., 1981: *Meso-scale Atmospheric Circulations.* Academic Press, 495 pp.

Batchelor, G. K., 1967: *An Introduction to Fluid Dynamics.* Cambridge University Press, 615 pp.

Chomaz, J. M., P. Huerre, and L. G. Redekopp, 1991: A frequency selection criterion in spatially developing flows. *Stud. Appl. Math.*, **84,** 119–144.

Chopra, K. P., 1973: Atmospheric and oceanic flow problems introduced by islands. *Advances in Geophysics,* Vol. 16, Academic Press, 297–421.

Drazin, P. G., and W. H. Reid, 1981: *Hydrodynamic Stability.* Cambridge University Press, 527 pp.

Etling, D., 1989: On atmospheric vortex streets in the wake of large islands. *Meteor. Atmos. Phys.*, **41,** 157–164.

Hannemann, K., and H. Oertel, 1989: Numerical simulation of the absolutely and convectively unstable wake. *J. Fluid Mech.*, **199,** 55–88.

Huerre, P., and A. M. Monkewitz, 1985: Absolute and convective instabilities in free shear layers. *J. Fluid Mech.*, **159,** 151–168.

——, and ——, 1990: Local and global instabilities in spatially developing flows. *Ann. Rev. Fluid Mech.*, **22,** 473–537.

Mattingly, G. E., and W. O. Criminale, 1972: The stability of an incompressible two-dimensional wake. *J. Fluid Mech.*, **51,** 233–272.

Merkine, L., and M. Shafranek, 1980: The spatial and temporal evolution of localized unstable baroclinic disturbances. *Geophys. Astrophys. Fluid Dyn.*, **16,** 174–206.

Nickerson, E. C., and M. A. Dias, 1981: On the existence of atmospheric vortices downwind of Hawaii during the HAMEC project. *J. Appl. Meteor.*, **20,** 868–873.

Pierrehumbert, R. T., 1984: Local and global baroclinic instability of zonally varying flow. *J. Atmos. Sci.*, **41,** 2141–2162.

Schär, C., and R. B. Smith, 1993: Shallow-water flow past isolated topography. Part I: Vorticity production and wake formation. *J. Atmos. Sci.*, **50,** 1373–1400.

Smith, R. B., 1989: Hydrostatic flow over mountains. *Advances in Geophysics,* Vol. 31, Academic Press, 1–41.

von Kármán, T., and H. Rubach, 1912: Über den Mechanismus des Flüssigkeits- und Luftwiderstandes. *Phys. Z.*, **13,** 49–59.